A halo model approach to the $21\mathrm{cm}$ and $\mathrm{Ly}\alpha$ cross correlation

Chang Feng*,[1] Asantha Cooray,[1] and Brian Keating[2]

[1]*Department of Physics and Astronomy, University of California, Irvine, CA 92697, USA*
[2]*Department of Physics, University of California, San Diego, CA 92093, USA*

We present a halo model-based approach to calculate the cross-correlation between 21cm HI intensity fluctuations and Lyα emitters (LAE) during the epoch of reionization (EoR). Ionizing radiation around dark matter halos are modeled as bubbles with the size and growth determined based on the reionization photon production, among other physical parameters. The cross-correlation shows a clear negative-to-positive transition, associated with transition from ionized to neutral hydrogen in the intergalactic medium during EoR. The cross-correlation is subject to several foreground contaminants, including foreground radio point sources important for 21cm experiments and low-z interloper emission lines, such as Hα, OIII and OII, for Lyα experiments. Our calculations show that by masking out high fluxes in the Lyα measurement, the correlated foreground contamination on the 21cm–Lyα cross-correlation can be dramatically reduced. We forecast the detectability of 21cm–Lyα cross-correlation at different redshifts and adopt a Fisher matrix approach to estimate uncertainties on the key EoR parameters that have not been well constrained by other observations of reionization. This halo model-based approach enables us to explore the EoR parameter space rapidly for different 21cm and Lyα experiments.

PACS numbers:

I. INTRODUCTION

The early Universe, initially filled with hot plasma, became neutral as hydrogen ions captured electrons that were decoupled from cosmic microwave background (CMB) photons at a redshift of 1100. A cosmic "dark age" subsequently ensued in the Universe until the linear density fluctuations seeded by inflation were amplified, forming the first stars and galaxies [1]. The X-rays from mini quasars and ultra-violet radiation from the massive stars in first-light galaxies heated and ionized the neutral hydrogen and the Universe gradually transformed from completely neutral to fully ionized during the epoch of reionization (EoR). Today the EoR still remains largely unexplored since signatures imprinted on the intergalactic medium (IGM) in the early Universe are too faint to be detected.

The physical processes present during EoR is of extreme importance to our understanding of the Universe and the structure that formed in it. The clustering of neutral hydrogen (HI) down to the Jeans length scale contains a wealth of information about certain fundamental physics, including dark matter. The HI tomography is not subject to small-scale physical effects like photon diffusion damping present in the CMB power spectrum. The timing and duration of EoR can help interpret other cosmological measurements, such as the kinetic Sunyaev-Zel'dovich (kSZ) effect [2]. Moreover, some exotic physics such as primordial magnetic fields [3] and decaying dark matter [4] could be probed during EoR. To date, the neutral fraction during the EoR was measured from quasar absorption spectra [5] and Lyα forest luminosity func-

tion [6–8] around $z \sim 6$. Another important quantity of the EoR, the Thomson scattering optical depth, is constrained to $\tau = 0.088 \pm 0.014$ by WMAP [9] and $\tau = 0.058 \pm 0.012$ by Planck satellites [10].

The best way to measure the HI content prior to and during reionization is through the 21cm HI fine-structure spin-flip transition. A number of experiments have been targeting the 21cm emission, such as the Low Frequency Array (LOFAR) [11], the Murchison Widefield Array (MWA) [12], the Precision Array for Probing the Epoch of Reionization (PAPER) [13], the Hydrogen Epoch of Reionization Array (HERA) [14] and the Square Kilometre Array (SKA) [15]. The redshifted 21cm emission is contaminated by both galactic and extragalactic foregrounds which consist of galactic synchrotron, supernovae remnants, free-free emission and radio point sources [16]. The Galactic synchrotron emission is the dominant contribution since it is three to four orders of magnitude stronger than the background brightness temperature fluctuations. By performing a component separation or subtracting the 21cm foreground, the 21cm brightness fluctuations could be measured [17]. This, however, relies on the reliability of the foreground estimation. The radio point sources are also thought to be another foreground issue for 21cm experiments, but this signal is very likely to be a subdominant contamination [18]. The expected 21cm signal is at the level of 10 mK^2 at $k = 0.3~\mathrm{Mpc}^{-1}$ [19], while recent measurements from PAPER set a 2σ upper limit as 22.4 mK^2 in the range $0.15 < k < 0.5~h\,\mathrm{Mpc}^{-1}$ at $z = 8.4$ [20].

During the EoR the ultraviolet Lyα emission was created by the first stars and galaxies. The Lyα background traces the underlying dark matter distribution and also affects the spin temperature distribution. By directly measuring the Lyα emissions, we get an additional observable on EoR physics as well [21]. However, the Lyα

*chang.feng@uci.edu

background is contaminated by low-z foregrounds, such as Hα at $z = 0.5$, OIII at $z = 0.9$, and OII at $z = 1.6$. These low-z components are much brighter than Lyα, precluding a clean detection. On the other hand, such low-z foregrounds can be easily masked out since they are very bright [22, 23]. Therefore, a simple masking procedure would recover the genuine Lyα background from experiments.

The 21cm and Lyα emission is anti-correlated at large angular scales since they originate from IGM and galaxies, respectively, and ionized bubbles around Lyα galaxies are devoid of HI that is seen with 21cm experiments. The transition in the cross-correlation from negative to positive indicates a characteristic size for the average of HII regions around halos. Thereby the cross-correlation between 21cm and Lyα can be viewed as a complementary probe of EoR physics. The cross-correlation could be more advantageous in terms of foreground removal since the two sets of foregrounds aforementioned would be largely uncorrelated, potentially allowing a higher signal-to-noise detection and an easy confirmation of the EoR signature. Previously, the cross correlation between 21cm and galaxies was studied for 21cm experiments such as MWA and LOFAR using both analytical and numerical calculations [24–26], as well as for LOFAR and Subaru's Hyper Suprime-Cam (HSC) [27]. The cross-correlation between 21cm and CO/kSZ also shows a similar transition in the correlation sign [28, 29].

So far different approaches have been used to model reionization. The large scale N-body and radiative transfer simulations, while desirable, are challenging since it is computationally intensive due to the large dynamic range [30, 31]. Another approach involves semi-analytical/semi-numerical models by taking a halo catalog generated from N-body simulations and generating a reionization field by smoothly filtering the halo field [32, 33]. A more simplified idea of this semi-numerical simulation is to make the density field from Gaussian random variables instead of relying on the N-body simulations. The simulation can be done efficiently within a small box for EoR [19, 34]. However, this numerical solution becomes ineffective when the box is too large or the simulated epoch is far beyond the EoR when the spin temperature is much higher than CMB. An upgraded version of this implementation uses a very similar algorithm to extend to large boxes [35]. Here, we apply a very simple ionizing bubble model [36] to the calculations of 21cm brightness temperature anisotropy and its cross-correlation with Lyα analytically, so we can quickly forecast the detectability of the signal for different combinations of 21cm and Lyα experiments, and explore the EoR parameter space without significant computational cost. This approach would be very beneficial when the cross-correlation measurements with different experiments and major foreground or instrumental issues need to be identified in the early stage of the development.

This paper is organized as follows. In Section II, we introduce the halo model for the ionizing bubble as well as the cross correlation. In Section III, the Lyα luminosity is discussed. Then we focus on the low-z foregrounds for both 21cm and Lyα measurements in Section IV and estimate signal-to-noise for the detectability of different experiments, as well as the uncertainties on the EoR parameters in Section V. We conclude in Section VI. We use the Planck cosmological parameters: $\Omega_b h^2 = 0.02230$, $\Omega_c h^2 = 0.1188$, $H_0 = 67.74 \, \text{km/s/Mpc}$, $Y_p = 0.249$, $\ln(10^{10} A_s) = 3.064$ at $k_* = 0.05 \, \text{Mpc}^{-1}$, $n_s = 0.9667$, and $\tau = 0.058$.

II. THEORETICAL MODEL OF THE CROSS CORRELATION

Here we describe the basic ingredients of our halo model. Since the mean ionizing fraction is not precisely constrained by current observations, we use the CAMB's instantaneous reionization model [37], i.e.,

$$\bar{x}_e(z) = \frac{1}{2}\Big[1 + \tanh\Big(\frac{(1 + z_{\text{re}})^{3/2} - (1 + z)^{3/2}}{\Delta y}\Big)\Big], \quad (1)$$

where the redshift z_{re} is derived from the optical depth τ today, i.e.,

$$\tau = \int_0^{\chi_{\text{re}}} d\ell \, n_e(\chi') \sigma_T , \quad (2)$$

and $\Delta y = 1.5\sqrt{1 + z_{\text{re}}}\Delta_z$. Here, σ_T is the Thomson cross section, the electron density is $n_e = (1 - 3/4Y_p)\rho_{b,0}/m_{\text{H}} a^{-3} x_e$, the comoving length $d\ell = a d\chi'$, Helium fraction is Y_p, proton mass is m_{H} and the mean neutral hydrogen fraction is $\bar{x}_H = 1 - \bar{x}_e$. One representative case for the ionizing fraction is demonstrated by Figure 1.

The 21cm brightness temperature can be split into two components $T_0(z)\psi(\mathbf{x}, z)$, in which the isotropic background temperature is

$$T_0(z) = 27\Big(\frac{1 - Y_p}{1 - 0.248}\Big)\Big(\frac{\Omega_b}{0.044}\Big)\Big[\Big(\frac{0.27}{\Omega_m}\Big)\Big(\frac{1 + z}{10}\Big)\Big]^{1/2} \, [\text{mK}], \quad (3)$$

and spatial fluctuation ψ is [38]

$$\psi(\mathbf{x}, z) = \bar{x}_H(1 + \delta_x)(1 + \delta) = \bar{x}_H(1 + \delta_x + \delta + \delta_x\delta) + ... \quad (4)$$

Here δ_x is the density contrast of ionizing field (x). For the 21cm field, we only consider the signals from IGM since galaxy contributions are 10^{-4} times smaller [39], and model the ionizing field with "bubbles" [38]. From Eq. (4), the two-point correlation functions for ionizing and matter density contrasts are $\langle\delta_x\delta_x\rangle = \xi_{xx}/\bar{x}_H^2$, $\langle\delta_x\delta\rangle = \xi_{x\delta}/\bar{x}_H$, and $\langle\delta\delta\rangle = \xi_{\delta\delta}$.

The auto-correlation function of the isotropic 21cm spatial fluctuation field is [40, 41]

$$\xi_{\psi\psi} = \xi_{xx}(1 + \xi_{\delta\delta}) + \bar{x}_H^2\xi_{\delta\delta} + \xi_{x\delta}(2\bar{x}_H + \xi_{x\delta}) + \xi_{x\delta x\delta}. \quad (5)$$

We neglect the redshift distortions and make use of the fact that the spin temperature is significantly higher than
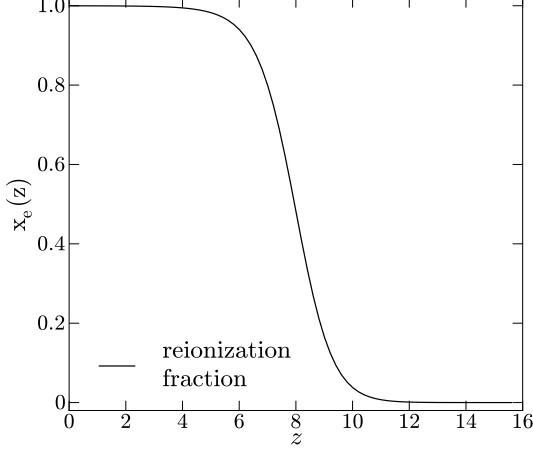
and its number density is

$$n_b(\mathbf{x}) = \bar{n}_b(1 + b\delta_L(\mathbf{x})), \tag{11}$$

where the density contrast δ_L is the matter density δ smoothed by a top-hat window of radius R. The top hat window in Fourier space is

$$\bar{W}_R^n(k) = \frac{1}{\bar{V}_b^n} \int_0^\infty dR P(R)[V_b(R)W(kR)]^n. \tag{12}$$

The shape factor for the ionizing field x is defined as

$$X_l^{(x)}(k, M, z) = \bar{x}_H \ln \bar{x}_H b_{\text{bubble}} \bar{W}_R(k) u_1, \tag{13}$$

with the bubble bias given by

$$b_{\text{bubble}} = \frac{1}{\bar{n}_b} \int_{M_{\text{th}}}^\infty b(M, z) \frac{dn}{d\ln M} \frac{dM}{M}. \tag{14}$$

Here, u_1 is the Fourier transform of the NFW profile [43], i.e., $u_1 = M/\bar{\rho}_m u$. The NFW Fourier transform is

$$u(k, M, z) = \frac{1}{M} \int_0^{r_{\text{vir}}} dr 4\pi r^2 \frac{\sin kr}{kr} \rho_{\text{NFW}}, \tag{15}$$

which is derived from a standard NFW profile

$$\rho_{\text{NFW}} = \rho_s \left(\frac{r}{r_s}\right)^{-1} \left(1 + \frac{r}{r_s}\right)^{-2}. \tag{16}$$

The detailed discussions of ρ_s, r_s and r_{vir} can be found in Ref. [44].

The 1-halo term of the 21cm field [45, 46] is

$$\begin{aligned}
P_{\psi\psi}^{(1h)} &= P_{xx}^{(1h)} + \bar{x}_H^2 P_{\delta\delta}^{(1h)} + 2\bar{x}_H P_{x\delta}^{(1h)} + P_{x\delta x\delta}^{(1h)} \\
&\simeq P_{xx}^{(1h)} + \bar{x}_H^2 P_{\delta\delta}^{(1h)} + P_{x\delta x\delta}^{(1h)},
\end{aligned} \tag{17}$$

where $P_{xx}^{(1h)} = (\bar{x}_e - \bar{x}_e^2)V_b \bar{W}_R^2$ and $P_{x\delta x\delta}^{(1h)} = (\bar{x}_e - \bar{x}_e^2)\tilde{P}_{\delta\delta}$. The term $P_{x\delta}^{(1h)}$ is zero since we assume the bubble is completely ionized. Here $\sigma_R^2 = \int dk k^2/2\pi^2 \bar{W}_R^2(k) P_{\delta\delta}(k)$ and $\tilde{P}_{\delta\delta} = P_{\delta\delta} V_b \sigma_R^2 / \sqrt{P_{\delta\delta}^2 + (V_b \sigma_R^2)^2}$. The 2-halo term can be easily calculated with the shape factor in Eq. (13).

On the other hand, the intensity mapping (IM) of Lyα emitters (LAEs) is a biased tracer of the same dark matter distribution, i.e., $\sim (1 + \delta_\eta)$. For simplicity, we use $\delta_{\text{Ly}\alpha} = \delta_\eta$. The cross correlation between 21cm and LAEs is

$$\xi_{\psi\eta} = \bar{x}_H(\xi_{\delta_\eta\delta} + \xi_{\delta_\eta x\delta}) + \xi_{x\delta_\eta}, \tag{18}$$

and the 3D power spectrum is

$$P_{\psi\eta} = \bar{x}_H(P_{\delta_\eta\delta} + P_{\delta_\eta x\delta}) + P_{x\delta_\eta}. \tag{19}$$

Here, the two-halo and one-halo terms are given by

$$\begin{aligned}
P_{\psi\eta}^{(2h)} &= \bar{x}_H(P_{\delta_\eta\delta}^{(2h)} + P_{\delta_\eta x\delta}^{(2h)}) + P_{x\delta_\eta}^{(2h)} \\
&\simeq \bar{x}_H P_{\delta_\eta\delta}^{(2h)} + P_{x\delta_\eta}^{(2h)}
\end{aligned} \tag{20}$$

FIG. 1: The ionization fraction with $z_{\text{re}} = 8.0$, $\tau = 0.058$ and $\Delta y = 6$. The redshift z_{re} is self-consistently solved when the optical depth τ and EoR duration parameter Δy are fixed.

CMB at $z < 10$ [42]. We Fourier transform the correlation function, assuming the quadratic terms are negligibly small. The 21cm power spectrum is

$$\begin{aligned}
P_{\psi\psi}^{(2h)} &= P_{xx}^{(2h)} + \bar{x}_H^2 P_{\delta\delta}^{(2h)} + 2\bar{x}_H P_{x\delta}^{(2h)} + P_{x\delta x\delta}^{(2h)} \\
&\simeq P_{xx}^{(2h)} + \bar{x}_H^2 P_{\delta\delta}^{(2h)} + 2\bar{x}_H P_{x\delta}^{(2h)}.
\end{aligned} \tag{6}$$

The power spectrum can be calculated from a halo model by describing HII regions as bubbles. The two-halo term of $P_{x\delta x\delta}$ is higher order and negligible [41].

The viral temperature of halo $T_{\text{vir}} = 5 \times 10^4$ K (suggested by [38]) sets the minimum halo mass,

$$\frac{T_{\text{vir}}}{10^4 \text{K}} = 1.1 \left(\frac{\Omega_m h^2}{0.15}\right)^{1/3} \left(\frac{1+z}{10}\right) \left(\frac{M_{\text{th}}}{10^8 M_\odot}\right)^{2/3}. \tag{7}$$

With this threshold mass, we can calculate the mean number density of bubble $\bar{n}_b = \int_{M_{\text{th}}}^\infty dM \frac{dn}{dM}$ and the average bubble size from $\bar{n}_b = -(\ln \bar{x}_H)/\bar{V}_b$. When it is compared to the predicted value

$$\bar{V}_b = \int dR P(R) V_b(R) = \frac{4\pi \bar{R}^3}{3} e^{9\sigma_{\ln R}^2/2}, \tag{8}$$

the bubble radius is constrained. The bubble radius R is assumed to satisfy a logarithmic distribution [25] as

$$P(R) = \frac{1}{R} \frac{1}{\sqrt{2\pi\sigma_{\ln R}^2}} e^{-\frac{1}{2}\left(\frac{\ln(R/\bar{R})}{\sigma_{\ln R}}\right)^2}. \tag{9}$$

Given the average volume and number density, the ionizing field is generated from a Poisson process

$$\langle x_e(\mathbf{x})\rangle = 1 - e^{-n_b(\mathbf{x})\bar{V}_b}, \tag{10}$$

and

$$P_{\psi\eta}^{(1h)} = \bar{x}_H(P_{\delta_\eta\delta}^{(1h)} + P_{\delta_\eta x\delta}^{(1h)}) + P_{x\delta_\eta}^{(1h)}$$
$$\simeq 0, \qquad (21)$$

respectively.

On small scales $P_{\delta_\eta x\delta}^{1h}$ cancels out the term $P_{\delta_\eta\delta}^{1h}$, so the summation is almost zero [25]. Also the large-scale information of $P_{\delta_\eta x\delta}^{2h}$ should be very negligible. With all of these approximations, the final power spectrum of the 21cm–Lyα cross-correlation is

$$P_{\psi\eta} \simeq P_{x\delta_\eta}^{(2h)} + \bar{x}_H P_{\delta_\eta\delta}^{(2h)}. \qquad (22)$$

The halo-model approach, i.e.,

$$P^{1h,XY}(k,z) = \int dM \frac{dn}{dM} X_l(k,M,z) Y_l(k,M,z) \qquad (23)$$

and

$$P^{2h,XY}(k,z) = P_{\text{lin}}(k,z) \int dM \frac{dn}{dM} b(M,z) \tilde{X}_l(k,M,z)$$
$$\int dM \frac{dn}{dM} b(M,z) \tilde{Y}_l(k,M,z), \qquad (24)$$

can be used to calculate each power spectrum in Eq. (22). In these equations, dn/dM is the mass function and $b(M,z)$ is the bias. The linear matter power spectrum is P_{lin}. We will work out the shape factors $X_l(k,M,z)$ and $Y_l(k,M,z)$ (or $\tilde{X}_l(k,M,z)$ and $\tilde{Y}_l(k,M,z)$) for Lyα in the next section.

III.   Lyα EMISSION

The UV radiations emitted from massive and short-lived stars can ionize the neutral hydrogen in the interstellar medium (ISM) in galaxies and the number of ionizing photons closely depends on the star formation rate (SFR). In this work we consider a SFR model which is consistent with numerical simulations. The fitted SFR [47] is

$$\frac{\text{SFR(M, z)}}{M_\odot \text{yr}^{-1}} = 2.8 \times 10^{-28} M^a \left(1 + \frac{M}{M_1}\right)^b$$
$$\left(1 + \frac{M}{M_2}\right)^d, \qquad (25)$$

where $a = 2.8$, $b = -0.94$, $d = -1.7$, $M_1 = 10^9 M_\odot$, and $M_2 = 7 \times 10^{10} M_\odot$.

The ionizing photons could escape the galaxies with a fraction $f_{\text{esc}}(M,z) = e^{-\alpha(M/M_\odot)^\beta}$ but the remains will ionize the hydrogen and 66% of the ionization will result in recombination process which produces Lyα photons. The dust in the ISM can also absorb the Lyα emissions

and the remaining fraction that survives the dust extinction is $f_{\text{Lya}}(z)$. The luminosity due to the recombination is then calculated as

$$L_{\text{rec}}^{\text{GAL}}(M,z) = 1.55 \times 10^{42}(1 - f_{\text{esc}}) f_{\text{Lya}} \frac{\text{SFR}}{M_\odot \text{yr}^{-1}}. \qquad (26)$$

The ionizing radiation can heat the gas so the process of hydrogen excitation and cooling produces Lyα emission as well. The luminosities due to excitation and cooling are

$$L_{\text{exc}}^{\text{GAL}}(M,z) = 4.03 \times 10^{41}(1 - f_{\text{esc}}) f_{\text{Lya}} \frac{\text{SFR}}{M_\odot \text{yr}^{-1}}, \qquad (27)$$

and

$$L_{\text{cooling}}^{\text{GAL}}(M,z) = 1.69 \times 10^{35} f_{\text{Lya}}(1 + \frac{M}{10^8})$$
$$(1 + \frac{M}{2 \times 10^{10}})^{2.1}(1 + \frac{M}{3 \times 10^{11}})^{-3}, \qquad (28)$$

respectively.

Besides these line emissions, the continuum produces Lyα photons through stellar radiation, free-free (ff), free-bound (fb) and two-photon (2γ) processes. Among these contributions, the stellar emission with a black-body spectrum below the Lyman-limit is dominant and its luminosity is

$$L_{\text{stellar}}^{\text{GAL}}(M,z) = 5.12 \times 10^{40} f_{\text{Lya}} \frac{\text{SFR}}{M_\odot \text{yr}^{-1}}. \qquad (29)$$

Our calculation takes all of these continuum lines into account and the detailed line luminosity can be found in Ref. [47].

The total Lyα luminosity $L(M,z)$ from galaxy is a summation of all the above components and the shape factor for Lyα field is

$$X_l(k,M,z) = \frac{L(M,z)}{4\pi D_L^2} y D_A^2 u(k,M,z). \qquad (30)$$

Here the conversion factor from frequency to comoving distance is $y = d\chi/d\nu = \lambda/(ca^2)d\chi/dz$, λ is the line rest frame wavelength, D_L and D_A are luminosity and angular comoving distances. The mean Lyα intensity varies at different redshifts as

$$\bar{I}_{\text{Lya}}(z) = \int_{M_{\text{min}}}^{M_{\text{max}}} dM \frac{dn}{dM} \frac{L(M,z)}{4\pi D_L^2} y D_A^2, \qquad (31)$$

where $M_{\text{min}} = 10^8 M_\odot$ and $M_{\text{max}} = 10^{13} M_\odot$.

The escaped photons from galaxies can ionize the IGM which can also emit Lyα photons due to the recombination process. The recombination rate is

$$\dot{n}_{\text{rec}} = \alpha n_e n_{\text{HII}}, \qquad (32)$$

where $n_e = x_e n_b$, $n_{\text{HII}} = x_e n_b C$, $C = (1 - Y_p)/(1 - 3Y_p/4)$ and α is case A comoving recombination coefficient. The
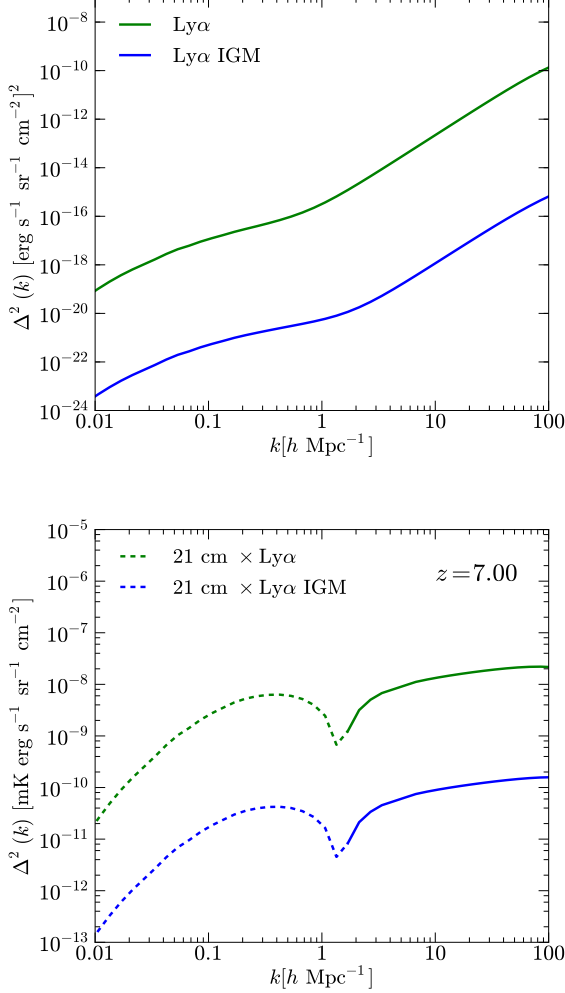
FIG. 2: The IGM contribution to both the auto- and cross-power spectra at $z = 7$. The IGM component is negligible, compared the galaxy. The dashed part is negative.

luminosity function of IGM is $L_{\rm rec}^{\rm IGM} = f_{\rm rec}\dot{n}_{\rm rec}E_{\rm Ly\alpha}$ and the fraction $f_{\rm rec}$ is spin temperature dependent. We show the contribution of IGM in Figure 2 and it is seen that the IGM contribution is negligible for both auto- and cross-power spectra.

Another IGM contribution to Lyα emission comes from the scattering of Lyn photons escaping from galaxies. From the previous calculations [22, 47, 48], it is found that the diffuse IGM contribution is a few orders of magnitude smaller than the galaxies. Therefore, we ignore this contribution to the overall Lyα signal.

IV. LOW-Z FOREGROUNDS

The Lyα emission at the EoR can be significantly contaminated by low-z foregrounds. The foreground at z_f projected onto the source plane z_s becomes anisotropic

since the wave vector of the foreground power spectrum in Fourier space becomes $\mathbf{k}_{f\to s} = (\chi_s/\chi_f k_\perp,\, y_s/y_f k_\parallel)$ which is not radially symmetric. The low-z foregrounds are identified as Hα [6563 $\mathring{A}$, $z = 0.5$], OIII [5007 $\mathring{A}$, $z = 0.9$], and OII [3727 $\mathring{A}$, $z = 1.6$] with luminosities $L_{H\alpha} = 1.3 \times 10^{41}\frac{\rm SFR}{M_\odot {\rm yr}^{-1}}$, $L_{OII} = 7.1 \times 10^{40}\frac{\rm SFR}{M_\odot {\rm yr}^{-1}}$ and $L_{\rm OIII} = 1.3 \times 10^{41}\frac{\rm SFR}{M_\odot {\rm yr}^{-1}}$. The low-$z$ star formation rate is exclusively modeled as

$$\frac{{\rm SFR(M,z)}}{M_\odot {\rm yr}^{-1}} = 10^{a+bz}\Big(\frac{M}{M_1}\Big)^c\Big(\frac{M}{M_2}\Big)^d \qquad (33)$$

for the foreground line emissions. This SFR model is fitted to the numerical simulations below $z = 2$ and the parameters are constrained as $a = -9.097$, $b = 0.484$, $c = 2.7$, $d = -4.0$, $M_1 = 10^8 M_\odot$ and $M_2 = 8 \times 10^{11} M_\odot$ [23].

The projected power spectrum of the foreground is then expressed as

$$P_{f\to s}(k_\perp, k_\parallel, z_s) = \Big(\frac{\chi_s}{\chi_f}\Big)^2 \frac{y_s}{y_f} P(k_f, z_f) \qquad (34)$$

and $k_f = \sqrt{(\chi_s/\chi_f)^2 k_\perp^2 + (y_s/y_f)^2 k_\parallel^2}$. In Figure 6, we show the unprojected and projected power spectra for Hα. OIII and OII show similar contours so are neglected. In Figure 4, the blue and red curves are radially averaged from the anisotropic power spectra.

In Figures 4 and 8, we show the linear power spectra for Lyα and the foreground lines Hα, OIII and OII with projection and with flux masking at redshifts $z = 7$ and 9. The projected foreground emissions are much higher than the Lyα lines. By selecting the brightest sources at the flux detection threshold and forming a mask, we can effectively remove those "hot" pixels which only account for a very tiny fraction of the sky coverage [22, 23]. As can be seen from Figure 10, we show the percentage of the removed pixels as the threshold flux changes. We find that a flux cut at $10^{-18}{\rm W/m^2}$ can significantly lower amplitudes of the foreground power spectra while only removing less than 0.1% of the pixels. Therefore, the flux masking procedure makes the low-z foregrounds negligible.

The synchrotron radiation dominates the 21cm signals but its smooth spectral feature can be used to isolate this component in frequency domain easily, also the galactic foregrounds are not correlated with extra-galactic line emissions at low-z. So we do not expect any noticeable cross correlations between galactic synchrotron and Lyα foregrounds. However, the radio point sources which are too faint to be resolved are indeed correlated with the low-z foregrounds within $0.5 < z < 1.6$, so this component would be picked up in the 21cm–Lyα cross correlation, making it not as systematic-free as expected. To estimate its contribution, we use the model in Refs. [50–52]. The model is described as

$$\delta_{\rm radio}(\mathbf{x}) = \Big(\frac{\partial B_\nu}{\partial T}\Big)^{-1} I_\nu^{\rm radio}\delta_g(\mathbf{x}) \qquad (35)$$
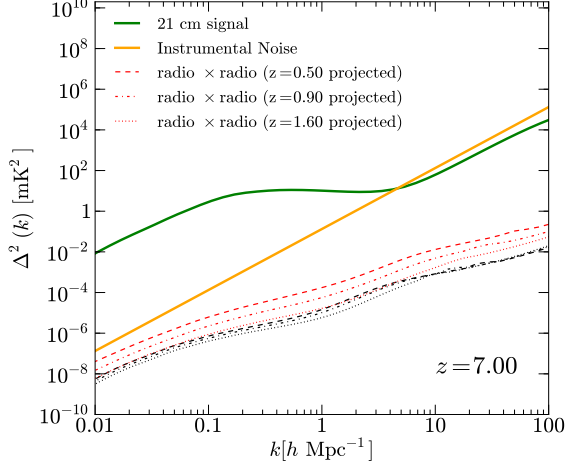
FIG. 3: The 21cm power spectrum at $z = 7$ (green). The radio flux cut is $S_{\rm cut} = 1\,{\rm mJy}$. The instrumental noise (orange) is derived from the SKA specification in Table I. The low-z foreground line and its projection are shown in black and red for each redshift when a Lyα foreground line is present. A spectral fitting scheme for the radio sources is assumed and the suppression factor is assumed to be 10^{-6} [49].
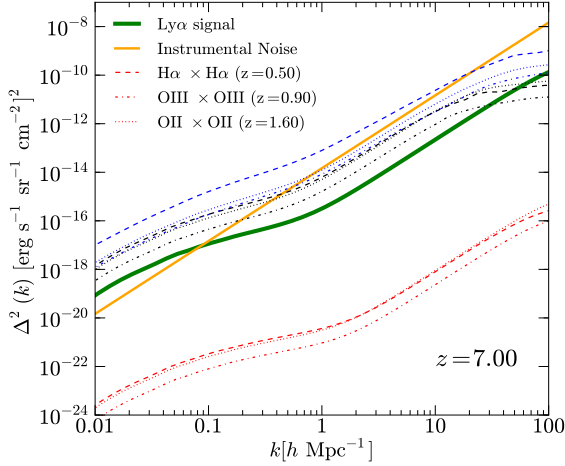

FIG. 4: The Lyα power spectrum at $z = 7$ (green). We show the low-z foreground power spectra with no projection (black), projection (blue) and masking (red). The instrumental noise (orange) is derived from the proposed CDIM specification listed in Table II.

based on the fact that the radio point source is a tracer of underlying density field. Here we have defined $I_\nu^{\rm radio} = \int_0^{S_{\rm cut}} dS S dN/dS$ and assume a flux limit $S_{\rm cut} = 1\,{\rm mJy}$ above which the radio point sources are bright enough to be resolved. The flux distribution is a simple power-law, i.e., $dN/dS = A(S/S_0)^\alpha$, where $A = 4\,{\rm mJy}^{-1}\,{\rm sr}^{-1}$, $S_0 = 880\,{\rm mJy}$ and $\alpha = -1.75$ [49]. Also, $\partial B_\nu/\partial T =$
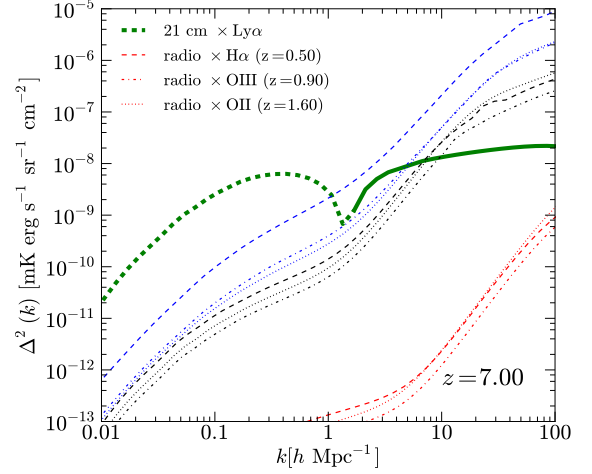

FIG. 5: The 21cm–Lyα cross-power spectrum at $z = 7$ (green) and the green dashed line indicates it is negative. We show the radio-line foreground cross power spectra with no projection (black), projection (blue) and masking (red). The radio flux cut is $S_{\rm cut} = 1\,{\rm mJy}$. The instrumental noise for the cross correlation is zero.

$99.27\,{\rm Jy}\,{\rm sr}^{-1}/(\mu{\rm K})x^4 e^x/(e^x{\text -}1)^2$ and $x = h\nu/k_b T_{\rm CMB} = \nu/56.84\,[{\rm GHz}]$. In Fourier space, the shape functions of the halo model for the radio sources are described as

$$X_l(k, M, z) = \frac{\sqrt{2N_c N_s u(k, M, z) + N_s^2 u^2(k, M, z)}}{\bar{n}_g} \tag{36}$$

and

$$\tilde{X}_l(k, M, z) = \frac{N_s u(k, M, z)}{\bar{n}_g}. \tag{37}$$

Here the central and satellite galaxy numbers are

$$N_c(M) = \frac{1}{2}\Big[1 + {\rm erf}\Big(\frac{\log_{10} {\rm M} - \log_{10} {\rm M}_{\rm min}}{\sigma_{\rm M}}\Big)\Big] \tag{38}$$

and

$$N_s(M) = \frac{1}{2}\Big[1 + {\rm erf}\Big(\frac{\log_{10} {\rm M} - \log_{10} 2{\rm M}_{\rm min}}{\sigma_{\rm M}}\Big)\Big]\Big(\frac{{\rm M}}{{\rm M}_{\rm s}}\Big)^{\alpha_{\rm s}}. \tag{39}$$

The mean galaxy number density is

$$\bar{n}_g(z) = \int dM n(M, z) N_g(M), \tag{40}$$

where $N_g(M) = N_c(M) + N_s(M)$. The parameters determined from luminosity and color dependence of galaxy clustering in the SDSS DR7 main galaxy sample are $M_{\rm min} = 10^9 M_\odot$, $\sigma_M = 0.2$, $M_s = 5 \times 10^{10} M_\odot$, and $\alpha_s = 1$ [53].

We estimate the radio foreground contributions at the Lyα foreground redshifts and the raw power spectra are a few orders of magnitude higher than the 21cm signal as revealed by [49, 54]. So the foreground suppression
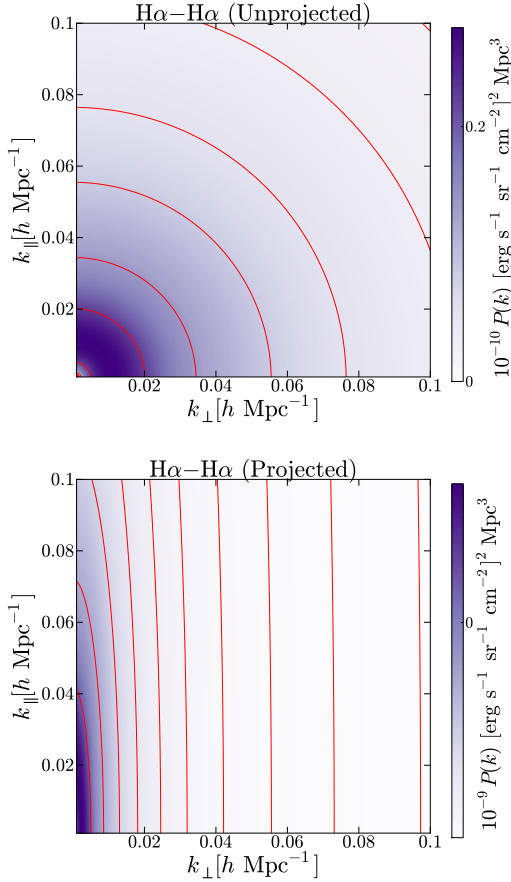
FIG. 6: The power spectrum projection of Hα at $z = 7$. OIII and OII power spectrum projections have similar patterns.

is very crucial and the spectral fitting procedure studied in [49] demonstrated that the radio foregrounds can be reduced by six orders of magnitude in map space and it has been validated that this is true from flux cut 0.1 mJy to 100 mJy. Thereby the radio foreground contamination becomes negligible and we show all the power spectra in Figures 3 and 7 at redshifts $z = 7$ and 9. We see that the resulting radio point sources have very negligible contaminating power on the 21cm measurements. Finally, we show the 21cm–Lyα cross-power spectra at redshifts $z = 7$ and 9 in Figures 5 and 9 with both foreground separation schemes incorporated.

V. FORECAST FOR THE EXPERIMENTS

In this section, we consider two experiments, Square Kilometre Array (SKA) and Cosmic Dawn Intensity Mapper (CDIM) [55, 56], and investigate the detectability of the 21cm–Lyα cross correlation with both instrumental noises and foregrounds. We list the experimental specifications in Tables I and II.

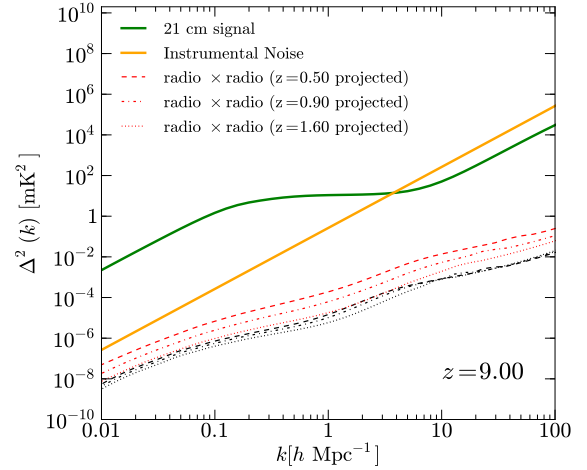The instrumental noise of 21cm experiment is entirely

FIG. 7: The 21cm power spectrum at $z = 9$ (green). The description of other lines is the same as Figure 3.
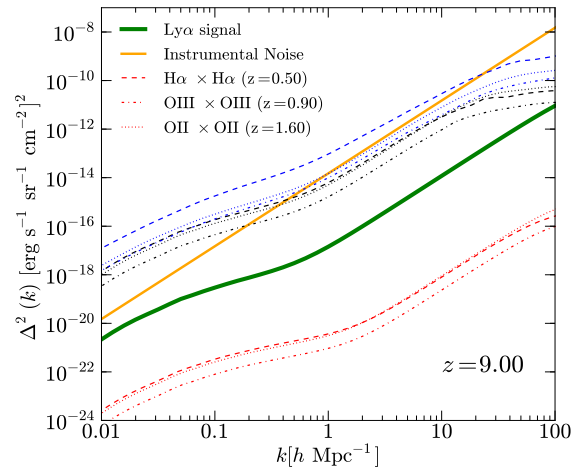

FIG. 8: The Lyα power spectrum at $z = 9$ (green). The description of other lines is the same as Figure 4.

determined by some key factors, such as integration time t_0, system temperature $T_{\rm sys}$, maximum baseline $D_{\rm max}$, collecting area $A_{\rm tot}$, antanna number N_a and frequency resolution $d\nu$. The noise is then given by

$$P_N^{\rm 21cm} = \chi^2 y \pi \left(\frac{\lambda D_{\rm max} T_{\rm sys}}{A_{\rm tot} N_a} \right)^2 \frac{1}{t_0}. \tag{41}$$

For the Lyα experiments, the noise is

$$P_N^{\rm Ly\alpha} = V_{\rm pix} \sigma_N^2, \tag{42}$$
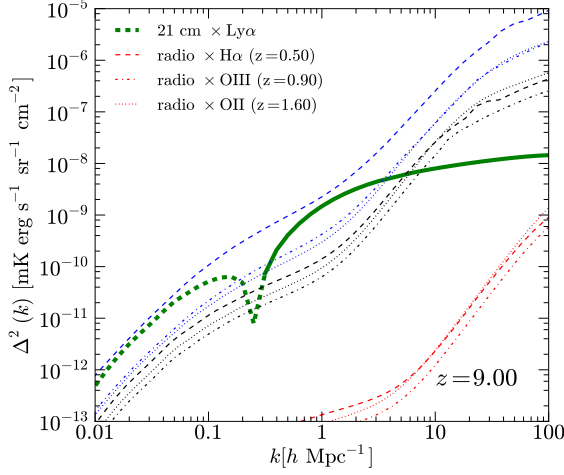
where the comoving volume subtended by the detector pixel

$$V_{\rm pix} = \chi^2 A_{\rm pix} y \delta_\nu \tag{43}$$

TABLE I: 21cm experiment

exp.	$\lambda^{\rm rest}$[m]	$D_{\rm max}$[m]	$T_{\rm sys}$[K]	t_0[hr]	$A_{\rm tot}$[m^2]	FOV[deg^2]	BW	$\delta\nu$	N_a	z
SKA1-LOW	0.21	1000	400	1000	925	13	18MHz	3.9kHz	433	8

TABLE II: Lyα experiment

exp.	$\lambda^{\rm rest}$[Å]	$\Omega_{\rm pix}$[″]	A_s[deg^2]	$\sigma_{\rm pix}$[erg s^{-1} cm^{-2} sr^{-1}]	$\lambda/\delta\lambda$	BW[μm]
CDIM	1216	1	300	3×10^{-6}	500	0.7-8.0

FIG. 9: The 21cm–Lyα cross-power spectrum at $z = 9$ (green). The description of other lines is the same as Figure 5.

FIG. 10: The flux threshold of Hα line at $z = 0.5$.

depends on the pixel area $A_{\rm pix}$ and frequency resolution δ_ν. The general Knox formula for the measured signal 21cm or Lyα is

$$\Delta P_{X,Y}(k,z) = \sqrt{\frac{\tilde{P}^2_{X,Y}(k,z) + \tilde{P}_{XX}(k,z)\tilde{P}_{YY}(k,z)}{N_m}},$$
(44)

and the number of modes in the bin k is $N_m = 2\pi k^2 \Delta k \frac{V_s}{(2\pi)^3}$. Here $X, Y = \{21\text{cm}, \text{Ly}\alpha\}$, the survey volume is $V_s = \chi^2 A_s y B_\nu$, A_s is the survey area and B_ν is the bandwidth (BW). For Lyα experiments, the minimum and maximum scales are determined by the survey and pixel areas. For 21cm, we normally consider modes at scales below $k = 10\,{\rm Mpc}^{-1}$ and get the minimum k from the total survey area. For the cross-correlation, the common k range is chosen from two experiments and the minimum volume between the 21cm and Lyα experiments is taken to calculate the number of modes. The noise- and foreground-included power spectra are formed as $\tilde{P}_{21\text{cm}} = P_{21\text{cm}} + P^N_{21\text{cm}} + P^{\rm radio}_{21\text{cm}}$, $\tilde{P}_{\text{Ly}\alpha} = P_{\text{Ly}\alpha} + P^N_{\text{Ly}\alpha} + P^{\rm low\text{-}z}_{\text{Ly}\alpha}$ and $\tilde{P}_{21\text{cm}-\text{Ly}\alpha} = P_{21\text{cm}-\text{Ly}\alpha} + P^{\rm radio-low\text{-}z}_{21\text{cm}-\text{Ly}\alpha}$. The k region is binned in log-space and we calculate the errors using Eq. (44) for each k-band.

In Figures 11, 12 and 13, we show all the power spectra and their band errors for 21cm and Lyα at $z = 7$ and 9. As can be seen from Figure 13, the anti-correlations between neutral hydrogen and galaxies can be probed at very high signal-to-noise ratios.

From the forecasted power spectra in Figure 13, we can further try to constrain the EoR parameters which are defined as $\mathbf{P} = \{\tau,\, \Delta y,\, \sigma_{\ln R}\} = \{0.058,\, 6.0,\, 1.0\}$. The Fisher matrix [57] is

$$F_{ij} = \sum_{k,z} \frac{1}{(\Delta\eta(k,z))^2} \frac{\partial \Delta^2(k,z)}{\partial p_i} \frac{\partial \Delta^2(k,z)}{\partial p_j}.$$
(45)

Here $\Delta\eta(k,z)$ is the error on the cross-power spectrum Δ^2 and p_i refers to any parameters in the set $\mathbf{P}$ and $\Delta^2 = k^3/(2\pi^2)P_{21\text{cm}-\text{Ly}\alpha}$. All the 1σ confidence levels as well as the likelihood functions in Figure 14 are calculated from the 21cm–Lyα cross-power spectra at $z = 7$ and 9. As seen from the figure, the bubble size can be constrained from the cross correlation while the errors on the optical depth and duration of the reionization transition are large. This is due to the fact that the cross correlation is proportional to $x_e(z)$, not $x_e^2(z)$ that the 21cm–21cm and 21cm–τ [38] are proportional to. Therefore, the cross-power spectrum at a single redshift is less sensitive to the reionization history. However, the
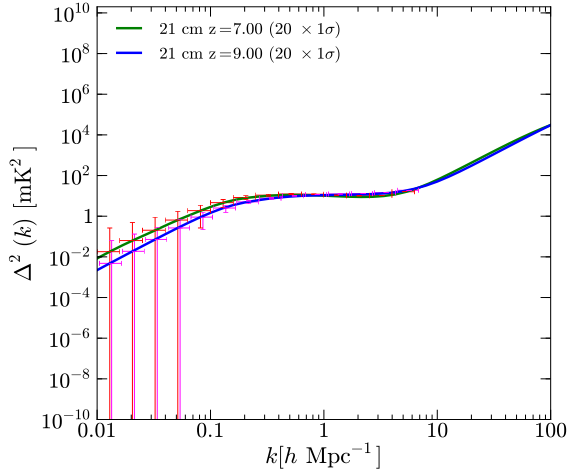
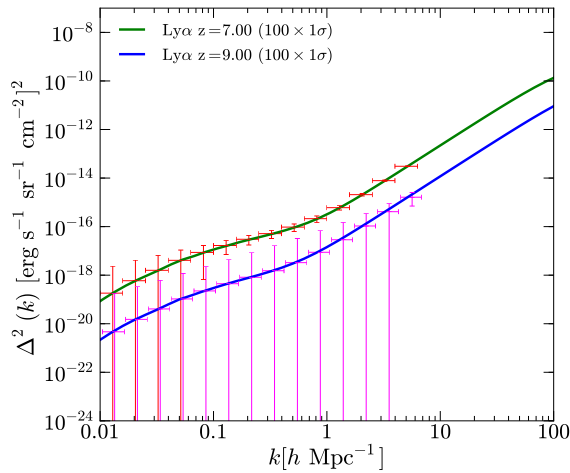FIG. 11: Forecast 21cm power spectra at $z = 7$ and 9 for experiment SKA.

FIG. 12: Forecast Lyα power spectra at $z = 7$ and 9 for experiment CDIM.

cross correlations at different redshifts might be able to break the degeneracies among the parameters so are useful as complementary probes to cosmological and astrophysical problems.

VI. CONCLUSION

In this work, we applied a bubble model to the computation of 21cm and Lyα cross correlation at the epoch

of reionization. Making use of the empirical relation between Lyα luminosity and mass for the line emissions, we also calculated the power spectra for Lyα. The
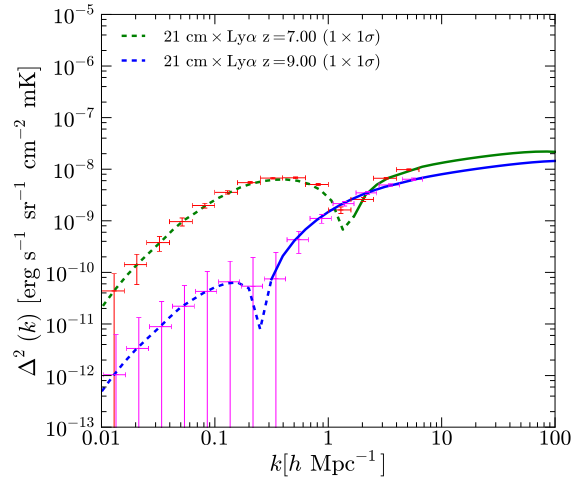

FIG. 13: Forecast 21cm–Lyα cross power spectra at $z = 7$ and 9 for experiments SKA and CDIM.

21cm–Lyα cross-power spectrum in this fast approach can reproduce the key features of the one made by detailed numerical simulations and we can use it to quickly assess the overall performance of the future EoR experiments.

The cross-correlation is contaminated by the low-z foregrounds for both 21cm and Lyα. We studied the radio galaxies for the 21cm experiments and Hα, OIII and OII line emissions for the Lyα experiments. All of these foregrounds could be a few orders of magnitude higher than the signals we are probing if the foreground mitigation is not incorporated. The map space spectral fitting can effectively remove the radio point source contaminations, while a flux masking for the intensity mapping experiments have been shown to be a good and easy foreground-removal method.

We take advantage of this efficient algorithm and estimate the errors on the EoR parameters τ, Δy and $\sigma_{\ln R}$ based on the Fisher matrix formalism. For other physical processes during the EoR, such as X-ray heating, supernovae explosion and shock heating, numerical simulations with these effects or an extension to this work should be devised and we will discuss them in the future work.
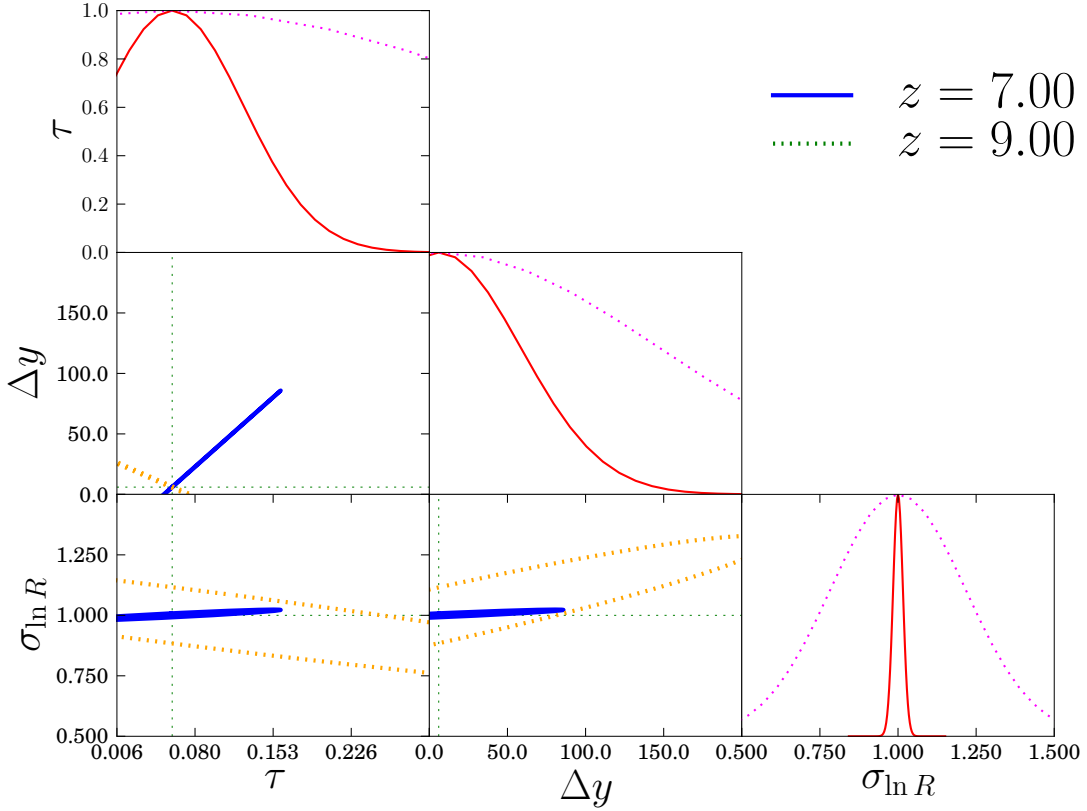
FIG. 14: The 1-σ confidence levels for the optical depth τ, the EoR duration Δy and the r.m.s. of the bubble size $\sigma_{\ln R}$ at $z = 7$ (solid) and 9 (dotted).

[1] A. Loeb and R. Barkana, Annu. Rev. Astron. Astrophys. **39**, 19 (2001), astro-ph/0010467.

[2] M. McQuinn, S. R. Furlanetto, L. Hernquist, O. Zahn, and M. Zaldarriaga, Astrophys. J. **630**, 643 (2005), astro-ph/0504189.

[3] D. R. G. Schleicher, R. Banerjee, and R. S. Klessen, Astrophys. J. **692**, 236 (2009), 0808.1461.

[4] S. R. Furlanetto, S. P. Oh, and E. Pierpaoli, Phys. Rev. D **74**, 103502 (2006), astro-ph/0608385.

[5] X. Fan, C. L. Carilli, and B. Keating, Annu. Rev. Astron. Astrophys. **44**, 415 (2006), astro-ph/0602375.

[6] A. Konno, M. Ouchi, Y. Ono, K. Shimasaku, T. Shibuya, H. Furusawa, K. Nakajima, Y. Naito, R. Momose, S. Yuma, et al., Astrophys. J. **797**, 16 (2014), 1404.6066.

[7] S. Malhotra and J. E. Rhoads, Astrophys J. **617**, L5 (2004), astro-ph/0407408.

[8] S. Malhotra and J. E. Rhoads, Astrophys J. **647**, L95 (2006), astro-ph/0511196.

[9] E. Komatsu, K. M. Smith, J. Dunkley, C. L. Bennett, B. Gold, G. Hinshaw, N. Jarosik, D. Larson, M. R. Nolta, L. Page, et al., Astrophys. J. Suppl. Ser. **192**, 18 (2011), 1001.4538.

[10] Planck Collaboration, R. Adam, N. Aghanim, M. Ash-down, J. Aumont, C. Baccigalupi, M. Ballardini, A. J. Banday, R. B. Barreiro, N. Bartolo, et al., Astron. Astrophys. **596**, A108 (2016), 1605.03507.

[11] M. P. van Haarlem, M. W. Wise, A. W. Gunst, G. Heald, J. P. McKean, J. W. T. Hessels, A. G. de Bruyn, R. Nijboer, J. Swinbank, R. Fallows, et al., Astron. Astrophys. **556**, A2 (2013), 1305.3550.

[12] S. J. Tingay, R. Goeke, J. D. Bowman, D. Emrich, S. M. Ord, D. A. Mitchell, M. F. Morales, T. Booler, B. Crosse, R. B. Wayth, et al., Publ. Astron. Soc. Aust. **30**, e007 (2013), 1206.6945.

[13] A. R. Parsons, D. C. Backer, G. S. Foster, M. C. H. Wright, R. F. Bradley, N. E. Gugliucci, C. R. Parashare, E. E. Benoit, J. E. Aguirre, D. C. Jacobs, et al., Astron. J. **139**, 1468 (2010), 0904.2334.

[14] D. R. DeBoer, A. R. Parsons, J. E. Aguirre, P. Alexander, Z. S. Ali, A. P. Beardsley, G. Bernardi, J. D. Bowman, R. F. Bradley, C. L. Carilli, et al., ArXiv e-prints (2016), 1606.07473.

[15] L. Koopmans, J. Pritchard, G. Mellema, J. Aguirre, K. Ahn, R. Barkana, I. van Bemmel, G. Bernardi, A. Bonaldi, F. Briggs, et al., Advancing Astrophysics with the Square Kilometre Array (AASKA14) 1 (2015),

1505.07568.

[16] S. R. Furlanetto, S. P. Oh, and F. H. Briggs, Phys. Rep. **433**, 181 (2006), astro-ph/0608032.

[17] A. Bonaldi and M. L. Brown, Mon. Not. R. Astron. Soc. **447**, 1973 (2015), 1409.5300.

[18] A. Liu, M. Tegmark, and M. Zaldarriaga, Mon. Not. R. Astron. Soc. **394**, 1575 (2009), 0807.3952.

[19] A. Mesinger, S. Furlanetto, and R. Cen, Mon. Not. R. Astron. Soc. **411**, 955 (2011), 1003.3878.

[20] Z. S. Ali, A. R. Parsons, H. Zheng, J. C. Pober, A. Liu, J. E. Aguirre, R. F. Bradley, G. Bernardi, C. L. Carilli, C. Cheng, et al., Astrophys. J. **809**, 61 (2015), 1502.06016.

[21] H. Jensen, P. Laursen, G. Mellema, I. T. Iliev, J. Sommer-Larsen, and P. R. Shapiro, Mon. Not. R. Astron. Soc. **428**, 1366 (2013), 1206.4028.

[22] A. R. Pullen, O. Doré, and J. Bock, Astrophys. J. **786**, 111 (2014), 1309.2295.

[23] Y. Gong, M. Silva, A. Cooray, and M. G. Santos, Astrophys. J. **785**, 72 (2014), 1312.2035.

[24] S. R. Furlanetto and A. Lidz, Astrophys. J. **660**, 1030 (2007), astro-ph/0611274.

[25] A. Lidz, O. Zahn, S. R. Furlanetto, M. McQuinn, L. Hernquist, and M. Zaldarriaga, Astrophys. J. **690**, 252 (2009), 0806.1055.

[26] J. S. B. Wyithe and A. Loeb, Mon. Not. R. Astron. Soc. **375**, 1034 (2007), astro-ph/0609734.

[27] D. Vrbanec, B. Ciardi, V. Jelić, H. Jensen, S. Zaroubi, E. R. Fernandez, A. Ghosh, I. T. Iliev, K. Kakiichi, L. V. E. Koopmans, et al., Mon. Not. R. Astron. Soc. **457**, 666 (2016), 1509.03464.

[28] A. Lidz, S. R. Furlanetto, S. P. Oh, J. Aguirre, T.-C. Chang, O. Doré, and J. R. Pritchard, Astrophys. J. **741**, 70 (2011), 1104.4800.

[29] V. Jelić, S. Zaroubi, N. Aghanim, M. Douspis, L. V. E. Koopmans, M. Langer, G. Mellema, H. Tashiro, and R. M. Thomas, Mon. Not. R. Astron. Soc. **402**, 2279 (2010), 0907.5179.

[30] I. T. Iliev, G. Mellema, U.-L. Pen, H. Merz, P. R. Shapiro, and M. A. Alvarez, Mon. Not. R. Astron. Soc. **369**, 1625 (2006), astro-ph/0512187.

[31] I. Iliev, M. Santos, A. Mesinger, S. Majumdar, and G. Mellema, Advancing Astrophysics with the Square Kilometre Array (AASKA14) 7 (2015), 1501.04213.

[32] O. Zahn, A. Lidz, M. McQuinn, S. Dutta, L. Hernquist, M. Zaldarriaga, and S. R. Furlanetto, Astrophys. J. **654**, 12 (2007), astro-ph/0604177.

[33] O. Zahn, A. Mesinger, M. McQuinn, H. Trac, R. Cen, and L. E. Hernquist, Mon. Not. R. Astron. Soc. **414**, 727 (2011), 1003.3455.

[34] A. Mesinger and S. Furlanetto, Astrophys. J. **669**, 663 (2007), 0704.0946.

[35] M. G. Santos, L. Ferramacho, M. B. Silva, A. Amblard, and A. Cooray, Mon. Not. R. Astron. Soc. **406**, 2421 (2010), 0911.2219.

[36] S. R. Furlanetto, M. Zaldarriaga, and L. Hernquist, Astrophys. J. **613**, 1 (2004), astro-ph/0403697.

[37] A. Lewis, Phys. Rev. D **78**, 023002 (2008), 0804.3865.

[38] P. D. Meerburg, C. Dvorkin, and D. N. Spergel, Astrophys. J. **779**, 124 (2013), 1303.3887.

[39] Y. Gong, A. Cooray, M. B. Silva, M. G. Santos, and P. Lubin, Astrophys J. **728**, L46 (2011), 1101.2892.

[40] M. Zaldarriaga, S. R. Furlanetto, and L. Hernquist, Astrophys. J. **608**, 622 (2004), astro-ph/0311514.

[41] S. R. Furlanetto, M. Zaldarriaga, and L. Hernquist, Astrophys. J. **613**, 1 (2004), astro-ph/0403697.

[42] R. M. Thomas and S. Zaroubi, Mon. Not. R. Astron. Soc. **410**, 1377 (2011), 1009.5441.

[43] J. F. Navarro, C. S. Frenk, and S. D. M. White, Astrophys. J. **462**, 563 (1996), astro-ph/9508025.

[44] C. Feng, A. Cooray, and B. Keating, ArXiv e-prints (2016), 1608.04351.

[45] M. J. Mortonson and W. Hu, Astrophys. J. **657**, 1 (2007), astro-ph/0607652.

[46] X. Wang and W. Hu, Astrophys. J. **643**, 585 (2006), astro-ph/0511141.

[47] M. B. Silva, M. G. Santos, Y. Gong, A. Cooray, and J. Bock, Astrophys. J. **763**, 132 (2013), 1205.1493.

[48] M. B. Silva, R. Kooistra, and S. Zaroubi, Mon. Not. R. Astron. Soc. **462**, 1961 (2016), 1603.06952.

[49] A. Liu, M. Tegmark, and M. Zaldarriaga, Mon. Not. R. Astron. Soc. **394**, 1575 (2009), 0807.3952.

[50] L. Gleser, A. Nusser, and A. J. Benson, Mon. Not. R. Astron. Soc. **391**, 383 (2008), 0712.0497.

[51] J. Singal, L. Stawarz, A. Lawrence, and V. Petrosian, Mon. Not. R. Astron. Soc. **409**, 1172 (2010), 0909.1997.

[52] P. Serra, A. Cooray, A. Amblard, L. Pagano, and A. Melchiorri, Phys. Rev. D **78**, 043004 (2008), 0806.1742.

[53] I. Zehavi, Z. Zheng, D. H. Weinberg, M. R. Blanton, N. A. Bahcall, A. A. Berlind, J. Brinkmann, J. A. Frieman, J. E. Gunn, R. H. Lupton, et al., Astrophys. J. **736**, 59 (2011), 1005.2413.

[54] D. Alonso, P. G. Ferreira, and M. G. Santos, Mon. Not. R. Astron. Soc. **444**, 3183 (2014), 1405.1751.

[55] J. Pritchard, K. Ichiki, A. Mesinger, R. B. Metcalf, A. Pourtsidou, M. Santos, F. B. Abdalla, T. C. Chang, X. Chen, J. Weller, et al., Advancing Astrophysics with the Square Kilometre Array (AASKA14) 12 (2015), 1501.04291.

[56] A. Cooray, J. Bock, D. Burgarella, R. Chary, T.-C. Chang, O. Doré, G. Fazio, A. Ferrara, Y. Gong, M. Santos, et al., ArXiv e-prints (2016), 1602.05178.

[57] J. C. Pober, A. Liu, J. S. Dillon, J. E. Aguirre, J. D. Bowman, R. F. Bradley, C. L. Carilli, D. R. DeBoer, J. N. Hewitt, D. C. Jacobs, et al., Astrophys. J. **782**, 66 (2014), 1310.7031.

VII. ACKNOWLEDGEMENTS